

Development of a High-Performance Low-Weight Hydraulic Damper for Active Vibration Control of the Main Rotor on Helicopters—Part 2: Preliminary Experimental Validation

Original

Development of a High-Performance Low-Weight Hydraulic Damper for Active Vibration Control of the Main Rotor on Helicopters—Part 2: Preliminary Experimental Validation / Bertolino, ANTONIO CARLO; Gaidano, Matteo; Smorto, Stefano; Giovanni Porro, Paolo; Sorli, Massimo. - In: AEROSPACE. - ISSN 2226-4310. - ELETTRONICO. - 10:10(2023), p. 868. [10.3390/aerospace10100868]

Availability:

This version is available at: 11583/2983868 since: 2024-02-14T10:34:40Z

Publisher:

MDPI

Published

DOI:10.3390/aerospace10100868

Terms of use:





This article is made available under terms and conditions as specified in the corresponding bibliographic description in the repository

Publisher copyright

(Article begins on next page)

Article

Development of a High-Performance Low-Weight Hydraulic Damper for Active Vibration Control of the Main Rotor on Helicopters—Part 2: Preliminary Experimental Validation

Antonio Carlo Bertolino ^{1,*} , Matteo Gaidano ¹ , Stefano Smorto ² , Paolo Giovanni Porro ²
and Massimo Sorli ¹ 

¹ Politecnico di Torino, 10129 Torino, Italy; matteo.gaidano@polito.it (M.G.); massimo.sorli@polito.it (M.S.)

² Elettronica Aster S.p.A., 20825 Barlassina, Italy; stefano.smorto@elaster.it (S.S.); paolo.porro@elaster.it (P.G.P.)

* Correspondence: antonio.bertolino@polito.it

Abstract: Vibrations generated by the main rotor-gearbox assembly in a helicopter are the principal cause of damage to cockpit instruments and crew discomfort in terms of cabin noise. The principal path of vibration transmission to the fuselage is through the gearbox's rigid support struts. This article is Part 2 of a two-part paper presenting an innovative solution involving the replacement of rigid struts with low-weight, high-performance active dampers for vibration control developed by Elettronica Aster S.p.A. Part 1 provided a comprehensive overview of the system layout obtained through a model-based design process and presented a thorough description of the adopted nonlinear mathematical model. Part 2 focuses on the physical realization of the damper and its dedicated experimental test bench. The mathematical model parameter fitting procedure is presented in detail, as it has been used to help in the definition and optimization of the control schemes and the verification of the expected performance. The experimental results obtained in Part 2 not only demonstrate the compliance of the active damper prototype with the acceptance tests outlined in the ATP but also provide compelling evidence reinforcing the promise of the presented solution for effective vibration reduction.



Citation: Bertolino, A.C.; Gaidano, M.; Smorto, S.; Porro, P.G.; Sorli, M. Development of a High-Performance Low-Weight Hydraulic Damper for Active Vibration Control of the Main Rotor on Helicopters—Part 2: Preliminary Experimental Validation. *Aerospace* **2023**, *10*, 868. <https://doi.org/10.3390/aerospace10100868>

Academic Editor: Sung N. Jung

Received: 1 September 2023

Revised: 28 September 2023

Accepted: 3 October 2023

Published: 5 October 2023



Copyright: © 2023 by the authors. Licensee MDPI, Basel, Switzerland. This article is an open access article distributed under the terms and conditions of the Creative Commons Attribution (CC BY) license (<https://creativecommons.org/licenses/by/4.0/>).

Keywords: active damper; vibration control; helicopter; electro-hydraulic servo-actuator

1. Introduction

Helicopters exhibit significantly higher vibration levels compared to fixed-wing aircraft. These vibrations primarily originate from the main rotor and gearbox assembly, but other factors, such as aeroelastic phenomena, mounting eccentricities, and blade-vortex interactions, contribute to the complex vibration pattern [1]. High vibration levels pose critical issues for both the instrumentation and the crew aboard helicopters. They diminish the ride quality experienced by occupants, leading to fatigue and long-term discomfort [2–4]. Additionally, these vibrations affect onboard instrument reliability and fatigue life [5,6].

In the past few decades, extensive efforts have been made to mitigate vibrations, resulting in the development of various solutions [7]. The traditional approach involves the incorporation of passive devices, such as tuned isolators and absorbers, strategically placed in specific locations to stabilize the structure [8]. However, these systems introduce substantial additional weight and increased aircraft drag. Moreover, they are tuned to specific frequencies and locations and lack adaptability to changes in flight conditions [8–10].

In recent years, active solutions have emerged as a promising avenue to enhance vibration reduction capabilities and improve adaptability to varying operational conditions [9]. Active devices generate forces that counteract the vibrations originating from the rotating elements of the helicopter, effectively minimizing their transmission to the fuselage. However, this approach necessitates actuating power and introduces increased complexity and reliability requirements to the system.

Following the introduction of active devices, numerous control techniques have been developed to actuate them using different strategies. These techniques aim to reduce vibration transmission, such as Active Control of Structural Response (ACSR) [9], or completely cancel vibrations at their source, such as High Harmonic Control [10] or Individual Blade Control [11]. Among the various locations, it has been found that the struts connecting the gearbox to the fuselage represent the primary path for vibration transmission, making them the ideal location for integrating active devices [7,12]. Typically, electromagnetic [7,13] or piezoelectric stack actuators [14,15] are placed in parallel with the rigid struts in order to generate an additional set of forces to compensate for vibrations, exploiting at the same time the stiffness of the rigid pylon.

Previous studies have explored an alternative solution, consisting of the entire replacement of the conventional struts with electro-hydraulic actuators to leverage the existing hydraulic circuitry present in helicopters [16,17]. However, these proposals did not gain practical application and widespread adoption because they faced practical limitations due to their excessive weight, space requirements, and very low power density in the order of 300 N/kg [10].

This paper positions itself within this context and presents an innovative alternative solution for active vibration control put forth by Elettronica Aster S.p.A. The proposed solution introduces an active damper comprised of a force-controlled electro-hydraulic servo-actuator (EHSA) housed within a compliant strut with controlled stiffness. The proposed design aims to replace the rigid struts traditionally used to support the main rotor/gearbox assembly. By employing this parallel layout, the internal EHSA can achieve high dynamics and power density while keeping the weight to a minimum, as it is solely responsible for generating additional forces, with the static load being borne by the flexible strut. The system design allows for easy adaptation to various helicopter platforms with diverse characteristics, such as rotor speed, number of blades, vibration forces, and so forth. The actuator design primarily focuses on effectively damping the first vibration frequency of the main rotor, which typically plays a significant role in the system's oscillations.

The novelty of the proposed solution lies in its fully integrated design, in which the EHSA cylinder serves not only as the hydraulic manifold but also accommodates the servo-valve and other functional and safety components, including the servo-valve, electro-valve, and bypass valve. The latter enables the damper to enter a bypass mode, deactivating force generation when vibration control needs to be suspended, such as in the event of a malfunction. In such cases, the active damper for vibration control (ADVC) becomes functionally transparent, with only the strut providing structural support and passive damping action based on its inherent design characteristics. This differs from the piezoelectric stack solution, which completely deactivates vibration control when power is lost, leaving the system without any damping. The compact design of the proposed solution facilitates achieving a high power density of more than 1250 N/kg while ensuring an extremely lightweight and space-efficient design, enabling the active damper to be installed in limited spaces and seamlessly integrated into pre-existing layouts, eliminating the necessity for structural modifications or adaptations when replacing the conventional struts. These factors are crucial for achieving desirable dynamics, reducing overall helicopter weight, optimizing fuel consumption, enhancing installation adaptability, and ultimately improving flight autonomy.

To be certified and installed onboard helicopters, the proposed ADVC must satisfy rigorous performance and safety requirements. The research program of which this paper presents the results aims to demonstrate the feasibility of implementing a competitive electro-hydraulic solution for active vibration control. The flowchart shown in Figure 1 graphically describes the methodology used throughout the research program.

After the definition of the case study and operative scenario, the required performances have been determined together with a document containing comprehensive acceptance and testing procedures (ATP) describing the specific tests that the actuator must successfully undergo to demonstrate its effectiveness in reducing vibrations. The system has then

been designed through an integrated approach exploiting linear and nonlinear dynamic modeling to simulate its response to the ATP tests to improve the system performance and design before manufacturing and testing on physical hardware. In parallel, a dedicated test rig has been designed to be able to reliably execute the tests in the conditions specified by the ATP. Finally, once the virtual prototyping and model-based design phases have been completed, the physical ADVC has been manufactured and tested. Initially, the prototype has undergone a series of tests aimed at verifying the expected behavior and validating the high-fidelity mathematical model, which has been subjected to a parameter-tuning process based on the experimental data. Hence, the tuned model has been exploited to tune the controller gains to optimize the system performance. Eventually, the physical ADVC has been tested according to ATP to certify its compliance with the initial requirements.

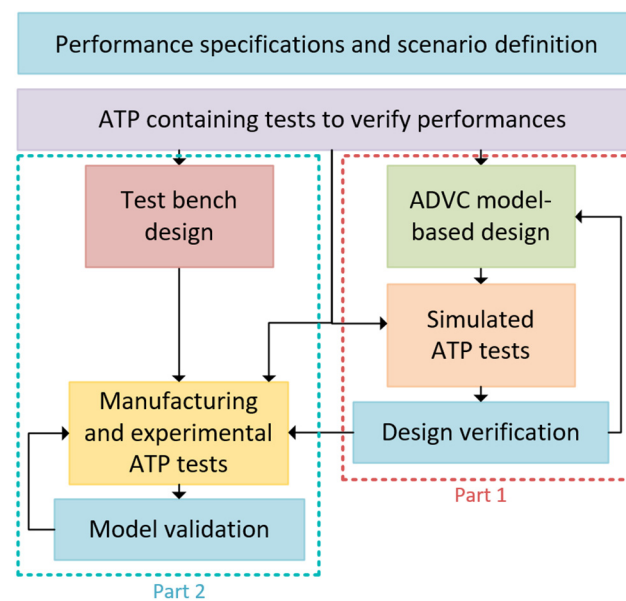


Figure 1. Conceptual flowchart of the research program, with the indication of the tasks described in Part 1 [18] and Part 2.

The work has been divided into two parts, as depicted in Figure 1. The first one [18] presents a comprehensive state of the art and introduces the proposed solution: it explains the conceptual architecture of the system and its working principle, together with a detailed description of the mathematical model used for the model-based design process. The acceptance and testing procedure (ATP) is outlined. The mathematical model is then used to preliminarily verify the design choices, simulating the system response to the ATP tests.

This paper provides the natural continuation of the research program, presenting the realized technological demonstrator and the physical implementation of a dedicated test bench appositely designed to perform ATP tests. The mathematical model has been fitted on the real prototype in order to validate the preliminary simulated results obtained in Part 1 [18]. Then, it has been used to gain additional insights into the system behavior and to inform the definition of control parameters to be used on the real equipment to pass ATP tests successfully. Finally, the physical prototype of the ADVC has undergone ATP tests on the test bench to validate its capabilities while ensuring compliance with the stringent performance requirements.

2. Case Study and ATP

The ATP, described in detail in [18], has been developed as a comprehensive document containing the testing and acceptance procedure to ensure the suitability of the ADVC for integration into aircraft systems. It encompasses a range of tests designed to verify both static and dynamic characteristics of the system.

The specific reference application for the ATP is a 15-seat medium-sized twin-engine helicopter with an estimated maximum take-off weight of 6000 kg. The combination of the number of blades and their rotational speed results in a vibratory disturbance at approximately 25 Hz within the cabin. Each strut experiences a portion of the fuselage mass, estimated at 500 kg. Building upon this information, the ATP incorporates various tests, from basic safety checks to application-specific tests aimed at verifying and ensuring the desired performance of the ADVC. In particular, it can be divided into:

- *Safety tests*, encompassing structural and hydraulic procedures to ensure the system's reliability during operations. These tests involve physical inspections, verification of maximum pressure and leakages, checks on mode switching, and other related assessments following applicable safety standards;
- *Static tests*, focused on assessing the external housing stiffness and determining the stall load capacity of the internal EHSA;
- *Dynamic tests*, evaluating the ADVC dynamic capabilities, including controllability and stability, disturbance rejection performance, and vibration reduction effectiveness at 25 Hz.

To conduct the acceptance tests, a dedicated test bench, which will be detailed in Section 4, has been designed and developed in order to be able to test the ADVC response to the case study condition defined as a reference for the ATP tests.

3. Damper Architecture and Physical Realization

The ADVC hydraulic circuit architecture has been thoroughly described in Part 1. Therefore, only the main concepts will be briefly recalled here for the sake of clarity, while the rest of the section will be devoted to describing the physical components employed.

As previously stated, the vibration control system addressed in this paper is composed of four of the proposed active dampers, which substitute the four conventional rigid struts that form the principal path for static and vibrational loads between the main rotor/gearbox assembly and the fuselage. Each ADVC consists of two main components arranged in a nested parallel configuration. The external compliant housing incorporates two hinges with revolute joints, a rigid hollow cylinder containing the EHSA, and a specially machined element that provides structural flexibility, acting as a spring with controlled stiffness. This latter element is in charge of guaranteeing a secure mechanical connection between the fuselage and the gearbox. Furthermore, it bears the static load, minimizing the internal parallel EHSA requested force and, consequently, its mass. In fact, it just must provide a high-frequency additional load to counteract the vibrating oscillations.

The result of the design phase is depicted in Figure 2, from which the main elements are visible. The body of the actuator is the manifold (shown in Figure 3) that accommodates all the components of the device and incorporates the installation flange, ensuring a highly compact design, as shown in the exploded view of Figure 4. In particular, the force signal, paramount to realizing the closed loop force control, is obtained through a load cell mounted directly on the threaded end of the rod, establishing the connection interface between the EHSA piston and the housing structure. With the goal of weight minimization, the load cell is of the miniaturized tension-compression type with a weight of 227 g and a nominal load of 44.5 kN.

To improve the performance of the control scheme with a feedforward branch, a Trans-Tek Inc. LVT (Linear Variable Transducer) [19] is integrated between the rod and the cylinder to measure their relative speed. Its design allows it to operate without external excitation, and the generated output voltage varies linearly with magnet velocity. The employed control scheme for the ADVC force loop is shown in Figure 5, in which a simple proportional-integral (PI) scheme with clamping anti-windup of the integral part is enhanced with the reading of the relative speed between the rod and the cylinder supplied by the LVT. This solution gives the possibility for the H/C designer to decide to compensate for the rod speed disturbance on the force control loop, integrating the PI scheme with the

definition of its custom G_{ff} block in the final implementation phase, depending on the considered specific application and helicopter class.

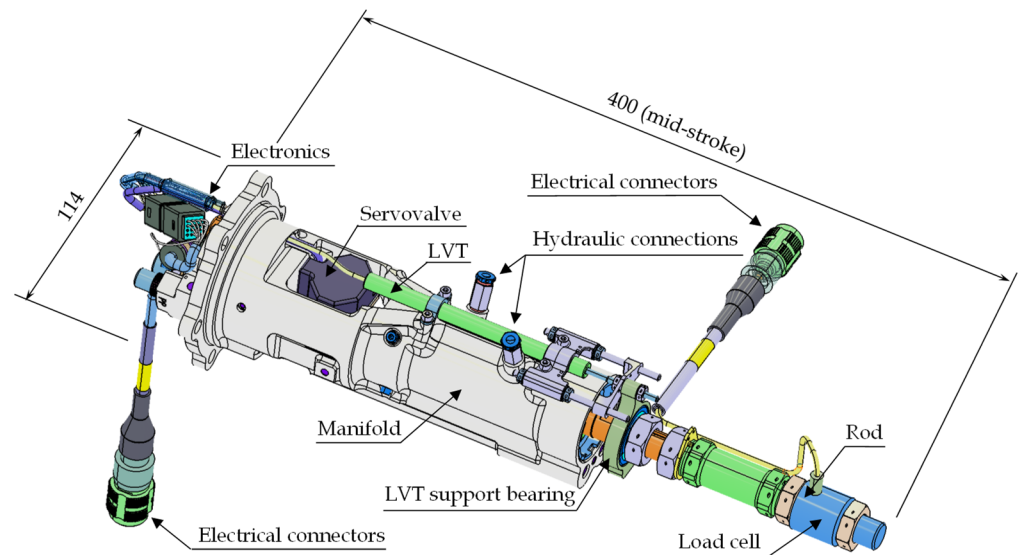


Figure 2. CAD of the internal EHSA, resulting from the design phase, with overall dimensions.



Figure 3. Manifold of the EHSA.

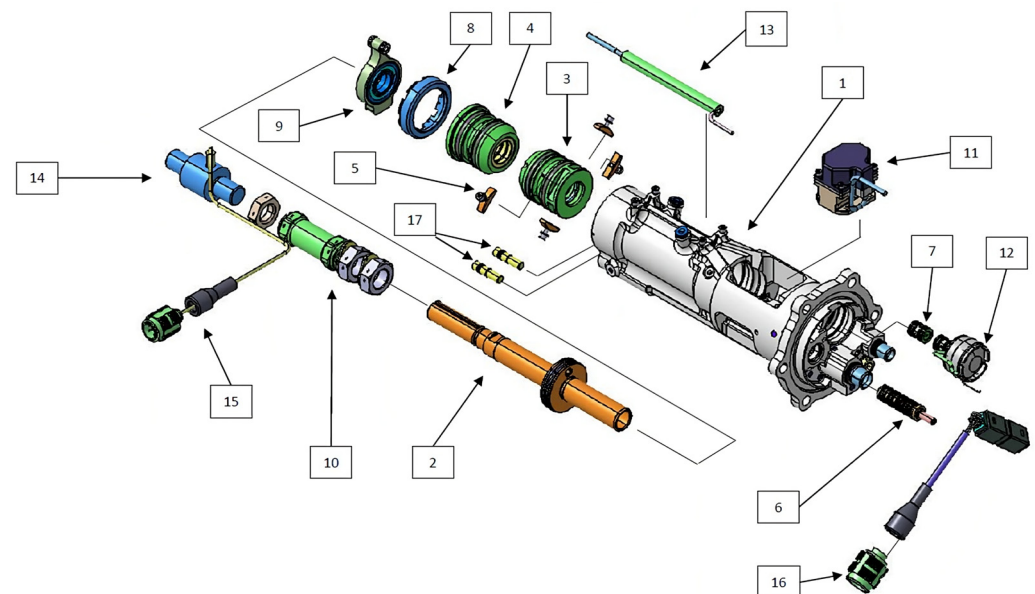


Figure 4. Exploded view of the internal EHSA: (1) Manifold, (2) Piston, (3) Inner gland, (4) Outer gland, (5) Segment gland, (6) Bypass valve, (7) Piloted solenoid valve, (8) Gland nut ring, (9) LVT support, (10) Joint tube, (11) EHSV, (12) Solenoid, (13) LVT, (14) Load cell, (15,16) MIL-DTL-38999 Series III electrical connections, (17) Relief valve.

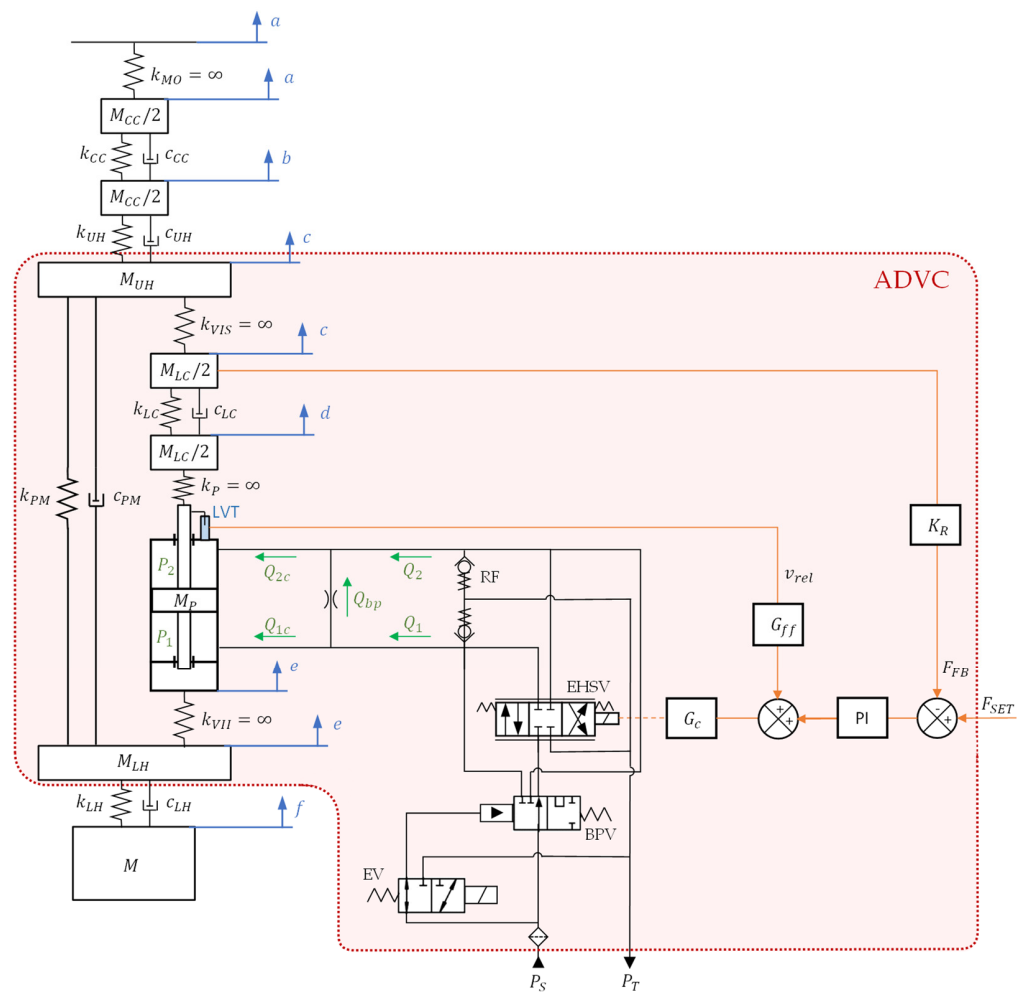


Figure 5. Aggregated representation of the EHSA hydraulic connections and control scheme inserted inside the mathematical model representation of the ADVC and its test bench (with reference to the extended model dissertation of Part 1 [18]).

The active force is generated by directing the flow of hydraulic oil into the actuator chambers by means of an electro-hydraulic servo-valve (EHSV), to which the flow is supplied through a 75 μm inlet filter. The EHSV, which regulates the flow proportionally to the current input command, is four ways and three positions (4/3) MOOG 30 Series flapper-nozzle 2-stages servo-valve with internal mechanical feedback [20]: this valve has been selected as it has a long history of performance in aerospace applications under severe environmental conditions, with endurance and pressure impulse fatigue requirements. In the ADVC application, the EHSV works within its functional limits and the generally accepted reliability envelope according to standard databases, such as NPRD-95 or NPRD-2016 (Nonelectronic Parts Reliability Data) [21], with 3.7944 failures per million flight hours considering continuous use. This value, translated in MTBF, largely exceeds the typical technical life of hydraulic actuators used on helicopters, i.e., in the tens of thousands of flight hours.

The hydraulic cylinder, designed and manufactured by Elettronica Aster, serves as the primary force generation element and is optimized to minimize internal friction. The two chambers are realized by the empty volume between the cylinder, the rod, and the glands. The latter, shown in Figure 6, guarantee both the ease of assembly of the system and the recovery and recirculation of the oil leaked in the interface with the rod during operations. This is realized thanks to the presence of an intermediate small chamber and recirculation ducts connected to the return pressure port.

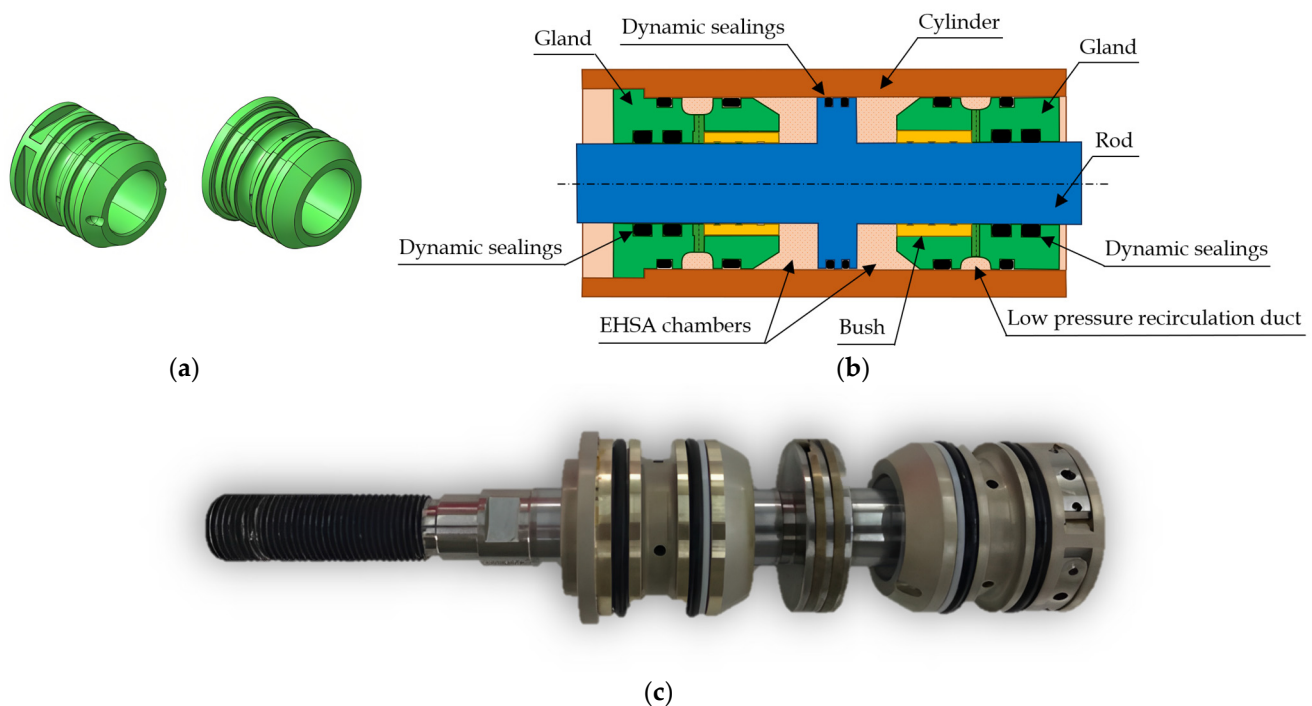


Figure 6. Glands that delimit the EHSA chamber volumes (a), schematic view of the rod assembly (b), and physical elements (c).

The glands feature a double stage of gaskets, composed of an inward contactless bush with a small clearance and gorges that help the lubrication of the ram and an outward low-friction aerospace dynamic sealing from Trelleborg Sealing Solution [22]. The intermediate oil duct guarantees a low pressure on the outwards dynamic sealings, reducing friction and leakage. The two chambers are isolated by two low-friction aerospace dynamic sealings on the piston from Precision Rings, Inc. [23]. In the case of overpressure in the actuator chambers, two relief valves from The Lee Company [24] are present to drain the oil in excess and stabilize the pressure. These valves are spring-preloaded to have a minimum opening pressure of 248 bar, with a nominal system pressure of 207 bar and a nominal flow point featuring 19.3 L/min at 310 bar.

A custom machined bypass valve (BPV), depicted in Figure 7, is interposed between the EHSV and the hydraulic cylinder: it allows the EHSV to be excluded and become transparent, isolating the cylinder from the rest of the EHSA and putting the two chambers in communication through a calibrated orifice, which allows the system to be more stable in the range of the null command and to avoid the possible hysteresis around the servo-valve zero position. This leads the vibration suppression functionalities to be inhibited and the ADVC to behave as a passive damping device with the external strut fulfilling its structural support and providing its inherent passive damping contribution, depending upon how it has been designed, exploiting the vibration-induced oil flow between the chambers and hydraulic resistances.

The bypass valve is hydraulically actuated. Therefore, if a drop in the supply pressure occurs, the valve closes under the action of its internal spring, isolating the system from the supply and connecting the two chambers.

The same scenario can occur if the electro-valve (EV), shown in Figure 8, is intentionally commanded to put the actuator in bypass mode or if there is a fault in the electrical system, which causes the electro-valve to deactivate. As it is an electrically commanded hydraulic valve connecting the bypass valve command line with either the supply or the return ports, its status directly affects the activation of the bypass valve.

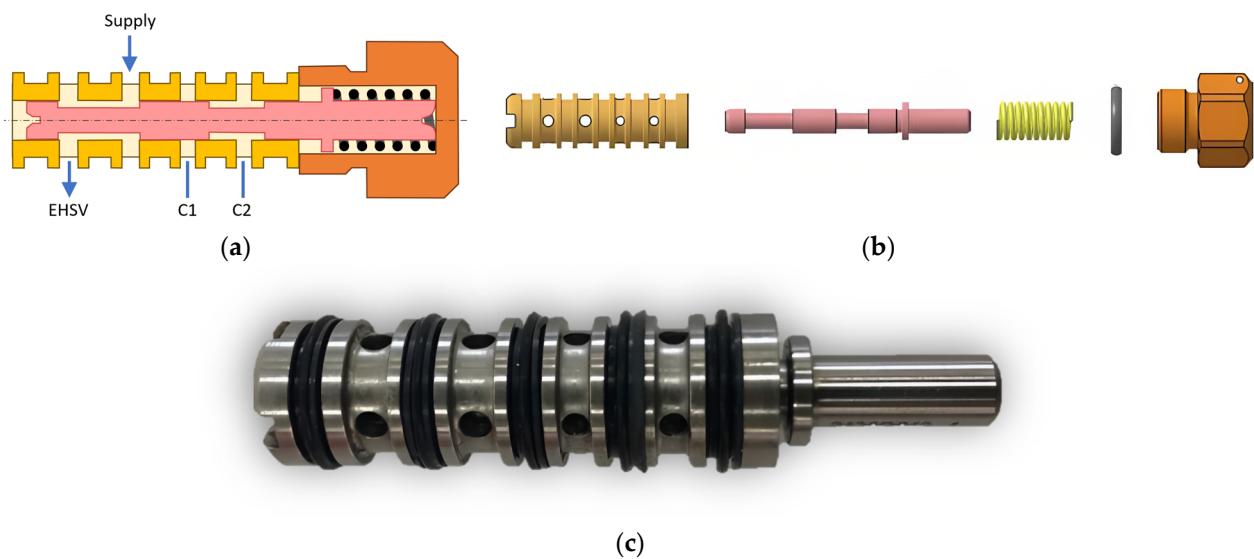


Figure 7. Bypass valve: (a) schematic section, (b) exploded view, (c) real assembly of the valve.

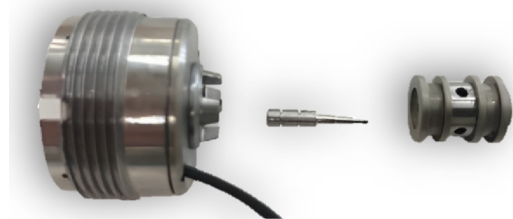


Figure 8. Solenoid valve exploded view.

Two relief valves (RF) connect the two chambers to the return (T) to avoid overpressures.

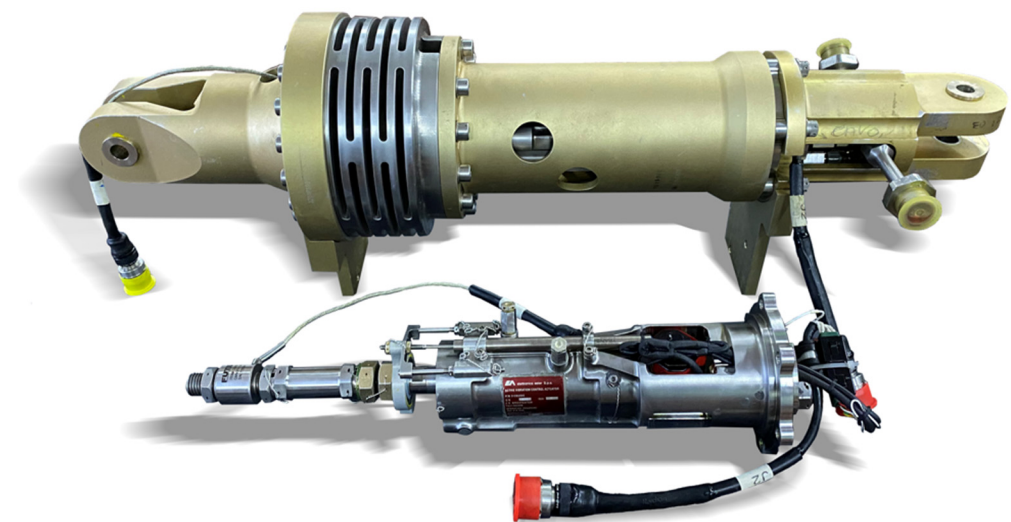
The electrical connections of the ADVC are provided by two connectors that meet all MIL-DTL-38999 Series III specifications. One connector is dedicated to the load cell, and the other is used to control the EHSV and the electro-valve and to receive information from the LVT. Force control is performed by the electronics within the ADVC itself. The internal load cell measures the force, which is then fed back to the control unit. The reference signal is received externally, and its generation lies beyond the scope of this paper. The ADVC is designed as a single force control unit with high performance. It allows the helicopter designer to optimize its configuration, taking advantage of the design flexibility provided by the compact EHSA dimensions. The integration of multiple ADVCs into the overall active vibration control system has not been addressed in this study.

The obtained assembled EHSA has a dry mass of approximately 5 kg with an overall mid-stroke length of 400 mm and a maximum width of 114 mm at the installation flange of the manifold (Figure 3). The main characteristics of the equipment are summarized in Table 1.

As previously mentioned, the EHSA is intended to be contained within an external hollow strut, which is in charge of providing the mechanical connection between the fuselage and the rotor/gearbox assembly and, at the same time, introducing controlled flexibility in the structure. The compliance of the strut is paramount as it allows the compensation of the vibration oscillations. The accurate design of the strut is not the primary objective of the current research project as it will be part of the design of the H/C, and it is expected to be realized in composite materials. In fact, the compliant strut shown in Figure 9 has been designed to represent a structure with controlled stiffness with the aim of testing and validation in the framework of a technological demonstrator. Therefore, it does not meet the standards of airworthiness (weight, dimensions, materials, and finishes), but it only has a functional goal.

Table 1. Technical and performance characteristics of the ADVC obtained from the design process.

Description	Value
<i>Hydraulic Power Supply</i>	
Hydraulic Fluid	MIL-PRF-83282
Supply pressure	202 ÷ 210 bar
Return pressure	5 ÷ 7 bar
Proof Pressure, Supply / Return	310 bar/155 bar
Burst Pressure, Supply / Return	515 bar/310 bar
Specification Actuator Flow Demand	Up to 5.7 L/min @ 195 bar
Servo-valve Rated Flow	12 L/min @ 207 bar
<i>Electrical Power Supply</i>	
Rated Voltage of Solenoid	28 VDC (16 ÷ 30 VDC)
Rated Current of Servo-Valve	10 mA Parallel
Solenoid Current Absorption	0.7 A max @ 28 VDC
<i>Functional and Performance Values</i>	
Stroke, Nominal/Maximum	± 0.5 mm/±10 mm
Nominal Operating Frequency	25 Hz
Stall Load, Nominal	±20 kN
Internal Actuator Dry Weight	5 kg
Total Dry Weight of ADVC	15.9 kg

**Figure 9.** EHSA prototype disassembled from the external compliant strut.

The strut consists of a lower eyelet, a rigid hollow cylinder housing the EHSA, an elastic joint, an upper eyelet, and two fins. The latter are additional appendices that, in normal working conditions, will not be present. However, they will be necessary for the test bench to allow differential laser measurements of the relative position of the two hinges.

The elastic component is an appositely machined element that gives flexibility to the structure, acting as a spring, designed to ensure minimal hysteresis and good linearity of the stiffness characteristic without having discontinuities in the stress inversion point, i.e., in the transition between tension and compression. It is sized according to the dynamic loads and static stresses that the strut must withstand even in case of passive operation, i.e., inactive damper.

4. Test Bench Layout

As previously stated, the ADVC prototype needs to be tested to verify its compliance with the ATP. Therefore, a dedicated test bench has been specifically designed to mimic the target scenario as closely as possible, resembling the vertical arrangement observed during flight where the helicopter body is suspended from the main rotor/gearbox assembly. The elements connecting these two parts are the struts, which, in this case, are the ADVCs.

The test bench is composed of four principal parts, which synergically work together to generate different input scenarios for the ADVC:

- the core of the test bench, shown in Figure 10b, which houses the ADVC during the tests;
- the hydraulic group, which supplies the hydraulic power to the ADVC and the test bench itself;
- the electric rack, containing the controller and the acquisition system both for the rig and the ADVC.
- the control unit, which is a computer connected to the electric rack that acts as an interface towards the operator, allowing him to run different tests and acquire data and information through a dedicated GUI (Graphical User Interface).

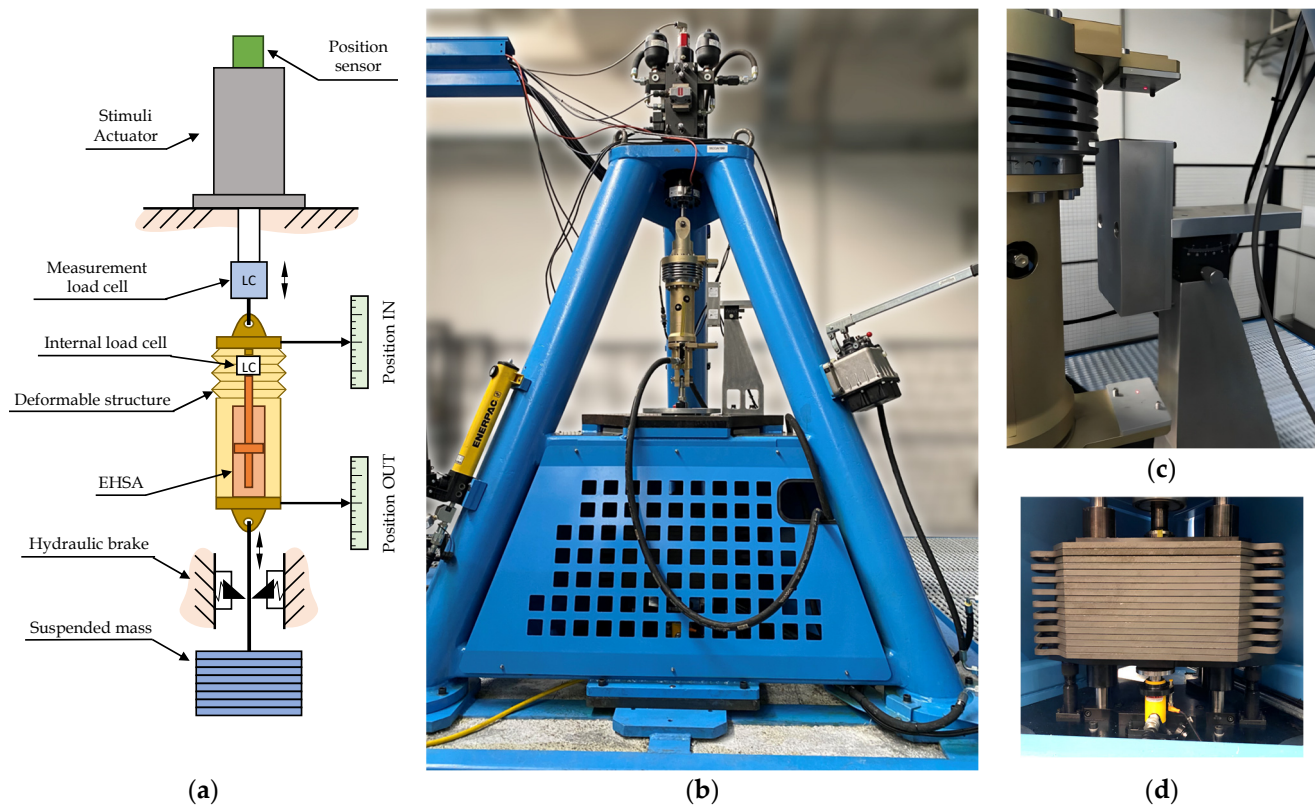


Figure 10. Experimental test bench designed to reproduce the test conditions specified in the ATP: (a) schematic representation highlighting the main components; (b) physical test bench; (c) laser measurement system; (d) suspended mass.

In this section, only the first element will be described and considered. To replicate the flight configuration, the ADVC is strategically positioned between a suspended mass, which represents a proportion of the cabin's mass typically supported by conventional struts and the stimuli actuator. The latter is an off-the-shelf electro-hydraulic position-controlled servo-actuator with hydrostatic bearing supports in charge of generating the vibratory disturbance to be mitigated, emulating the vibrations caused by the rotor and the gearbox. The entire connection chain supporting the mass is suspended and hung to the stimuli actuator, which is the sole component directly attached to the main rigid structure of the test bench, as depicted in Figure 10a. All the other components evolve in the vertical direction from the top to the bottom. The stimuli actuator is equipped with a coaxial LVDT to acquire its position and close the position control loop. Its servo-valve is mounted directly on the cylinder together with accumulators, helping the high-performance control of the actuator position at 25 Hz for an overall stroke of 50 mm and a stall load of 50 kN.

An additional load cell (HBM K-U10M-50K SB) with a nominal range of 50kN both in compression and in extension [25] is installed between the stimuli actuator's rod and the upper hinge of the ADVC, enabling accurate force measurement between the damper and the upper actuator.

To compute the transmissibility function, the vertical positions of the upper and lower hinges are captured by two Keyence LK-H082 laser sensors [26], shown in Figure 10c, exploiting the two additional fins connected to the hinges shown in Figure 9 and facilitating the determination of compliant structure elongation or compression resulting from the applied forces. The laser sensor supporting structure, observable in Figure 10c, has been accurately designed through FEM analyses to minimize the errors introduced by its oscillations due to the vibrations induced by both the stimuli actuator and the ADVC.

The suspended mass depicted in Figure 10d smoothly moves along vertical guides with low friction. The mass is composed of a stack of several metallic plates alternated with thin damping pads, which help to avoid plate resonance in the operative frequency range of the test bench. For safety considerations and to prevent uncontrolled mass oscillations, a hydraulic brake mechanism is incorporated into the system. A lift system composed of a hydraulic manual pump and a hydraulic jack allows the lifting or lowering of the mass during the installation phase of the ADVC in the test bench. A stem ending with an eyelet connection, which is also part of the mass weight, allows the connection with the lower hinge and constitutes the grabbing point of the brake.

The test bench framework is composed of a metallic pyramidal chassis with a triangular section. This layout has resulted from FEM analyses aimed to minimize undesirable structural deflections caused by the high-frequency vibratory load generated by the stimuli actuator. The chassis is then mounted on a seismic mass basement of approximately 6000 kg equipped with eight vibration isolation mounts and antivibration panels that prevent the transmission of the vibration generated by the test bench to the facility ground.

5. Mathematical Model Validation

The mathematical model has been thoroughly described in Part 1 [18] as it has been used for the model-based design process. In fact, thanks to a preliminary linear model and, subsequently, its advanced nonlinear evolution, the required performance of the ADVC has been met in accordance with the ATP specifications, leading to the layout depicted in Figure 2.

The mathematical model also carries out another task, which is supporting the real prototype optimization process involving the definition of control parameters. Furthermore, it has also been used to evaluate possible assembly issues and to check the correspondence of the measured signals with the expected simulated behavior. In this sense, the mathematical model assumed the role of a verification digital twin of the real equipment, its internal (not experimentally measured) signals being monitored throughout the setup phase, allowing a rapid and optimized convergence towards the desired performance.

The mathematical model comprises both the ADVC and the test bench, allowing the reproduction of the real test conditions in terms of given inputs and measured outputs. Although the stimuli actuator is not explicitly modeled, it is considered the disturbance input. Load cells, compliant elements (such as the strut), and hinges are represented as spring-damper systems. LuGre friction models are used in the sliding interfaces, i.e., between the rod and the cylinder and in the linear guides of the suspended mass. The electro-hydraulic servo-valve is modeled by leveraging the analogy with the electrical domain, employing a hydraulic resistance Wheatstone bridge [27,28], determined by the spool opening section [29]. The latter depends on the dynamics of the first-stage torque motor [30], which is represented as a second-order transfer function with hysteresis, null bias, current offset, non-linearities, and saturations. The leakages occurring in the EHSV and dynamic sealings, as well as friction levels, are calculated according to [31,32], while the bypass orifice is considered an orifice with turbulent flow conditions. Finally, the force generated by the internal EHSA is obtained by the differential pressure between

the actuator chambers, considering the temperature-dependent rheological properties of the oil. The electro-valve and bypass valve are not considered in the model, as only normal mode operations are simulated. The control electronics model represents the PI scheme with a feedforward branch of the real implementation, accommodating the transport delay introduced by the digital implementation, discretization errors, dead bands, saturations, anti-windup logics, and potential electromagnetic noise perturbations affecting the acquired signals.

The parameter tuning to fit the experimental data with the simulation results was fulfilled in three steps. First, the geometric dimensions involved in the model have been accurately experimentally verified, as well as all other measurable parameters. Then, the models of commercial components, such as the EHSV, have been fitted singularly with experimental data typical of the particular purchased component supplied by the manufacturer. Eventually, the remaining parameters have been estimated using signal acquisitions obtained by testing the entire ADVC on the dedicated test rig with the goal of gathering its main behavior and its characteristic features.

Due to its fully integrated nature by design, single components testing was not practical and not useful. In fact, it would have led to the loss of the strict interdependence of the involved components and, ultimately, to the estimation of wrong values for the uncertain parameters. Nevertheless, the effects of the various elements have been evaluated and partially isolated from each other, exploiting the suite of available sensors on the ADVC and the test bench.

The command and excitation signals have been conveniently defined to highlight specific characteristics of the tested equipment/component and to make the effect of certain parameters on the acquired signals stand out. This process involved a long phase of investigation and a deep understanding of the underlying physical behavior involved in the system. The parameter identification was formulated as a multi-objective constrained minimization problem in which the objective function was composed by the sum of the squared errors of the various simulated and experimental signals and where the independent variables were represented by the model parameters allowed to be varied within suitably meaningful ranges. Each evaluation of the cost function is represented by a single entire simulation of the model with a different set of parameters. The nonlinear least square Levenberg-Marquardt algorithm has been adopted as the optimization method. To speed up the identification process, a four-core parallel pool has been created, and the excitation signal has been reduced as much as possible.

The ADVC has undergone various kinds of tests before being verified against ATP procedures, such as open loop and closed loop experiments, to highlight diverse features of the system under test and to achieve a suitable suite of model parameters to enable more accurate simulations and performance predictions in the various scenarios. The key parameters of the system identified with the aforementioned procedure are listed in Table 2. The following paragraphs briefly describe the main tests performed to validate the model.

Table 2. Key identified parameters of the mathematical model.

Parameter	Value	Units
Hinges stiffness	557.7	kN/mm ²
Total suspended mass	524	kg
Servo-valve natural frequency	293	Hz
Servo-valve maximum flow @ 210 bar	7.1	L/min
Cylinder internal volume	21.3	cm ³
Force transducer natural frequency	11.25	kHz
Hydraulic oil bulk modulus	880	GPa

5.1. Servo-Valve

The EHSV model parameter-tuning process was carried out using experimental data from the certification tests supplied by the servo-valve manufacturer together with the

purchased component. In particular, two characteristic diagrams have been reproduced: the no-load flow and the pressure gain charts. In the model environment, the tests have been simulated by applying the same standard test conditions and testing system layouts, according to [33].

A dedicated model has been created containing only the EHSV component and two downstream volumes, independent and connected to the two output ports of the servo-valve. These volumes are necessary to obtain the downstream pressure from the flow rate, which is the output of the EHSV model. The pressure signal is, in fact, sent back as input together with the supply and tank pressure values to calculate the flow rate.

The no-load flow test has been reproduced, imposing a huge value for the downstream volumes to make the outlet pressure almost insensible to the inlet flow coming from the servo-valve, with ambient initial pressure. This reproduces the test conditions in which the outlet valves are open, and a constant rated pressure drop is maintained throughout the test [33]. With these conditions, a slow triangular current input signal is imposed on the servo-valve, spanning across the whole range of values up to the rated current in the positive and negative regions.

The pressure gain test is performed by plugging the output ports of the EHSV and measuring the generated pressures as the input current varies [33]. To reproduce this layout, the downstream volumes considered in the model have been sensibly reduced to take into account only the internal volumes of the servo-valve, simulating the plug of the ports. With these conditions, a slowly growing current input signal is imposed on the servo-valve until the lowest pressure reaches the tank value. Then, the current is reversed until the same condition is met on the other volume. Finally, the current is brought back to the null value to close the loop. The output of the test is the load pressure drop, i.e., the difference between the pressures measured in the two outlet volumes.

The certification test results provided by the manufacturer also contained the flow/current frequency response and the characteristic bandwidth. As detailed in [18], the servo-valve dynamics has been condensed into a unique second-order transfer function representing the first stage and spool dynamics of the servo-valve. The values of the natural frequency and damping factor have been estimated by fitting the amplitude and phase plots on the experimental ones and then feeding them directly into the model transfer function.

The obtained results are shown in Figure 11. The tuning process involved iteratively adjusting the model parameters to minimize the discrepancies between the experimental results and the predicted values obtained from the initial model. This iterative refinement allowed for a comprehensive and precise representation of the EHSV behavior, decoupling the EHSV effect from those of the other components in subsequent tuning processes.

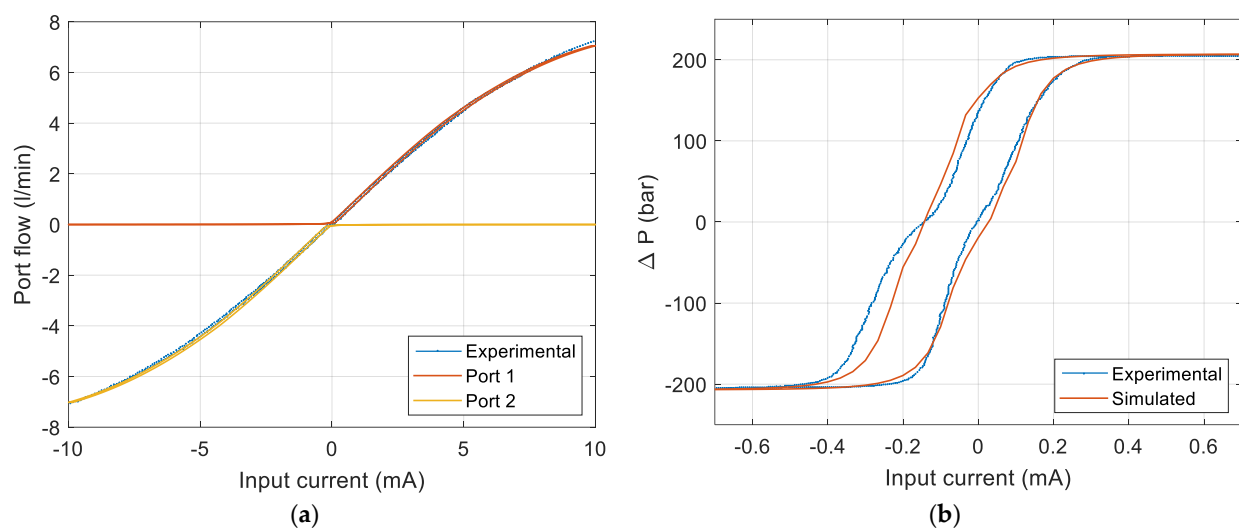


Figure 11. Results of the EHSV model parameters tuning on manufacturer's experimental tests of the real servo-valve component: (a) no-load flow chart, (b) pressure gain chart.

5.2. Test Bench Friction and Masses

Before performing validation tests on the ADVC itself to characterize its dynamical behavior, it is important to ensure that, as done for the servo-valve, the models of the surrounding components are sufficiently identified to allow easy decoupling of effects in successive component identification. With this goal in mind, another type of analysis has been carried out to characterize the test bench, excluding the ADVC. The latter has then been replaced by a rigid strut of known mass, shown in Figure 12a, with the aim of estimating the actual overall suspended mass attached to the ADVC and the friction occurring in its vertical guides. The stimuli actuator has been commanded with a sinusoidal position set with an amplitude of 1 mm and a sufficiently low frequency of 0.01 Hz so as not to incur excessive dynamic phenomena during measurements. Concurrently, the signal coming from the test bench load cell has been recorded together with the stimuli actuator's linear position.

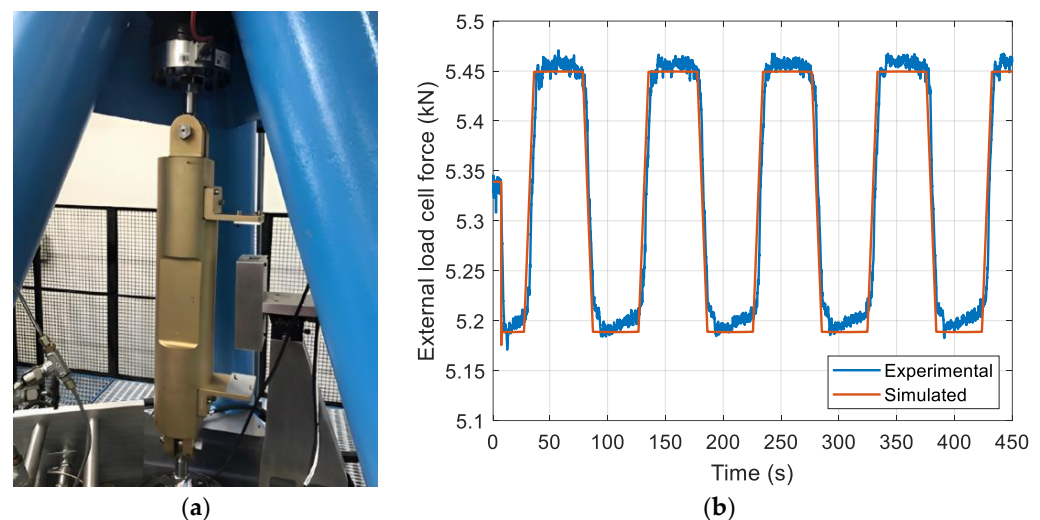


Figure 12. Test to estimate mass and linear guides friction: (a) test bench setup and (b) force signal read by the test bench load cell with simulated results obtained from the fitted model.

The results reported in Figure 12b allowed the evaluation of the total mass hung to the load cell and the guide rail friction contribution. In fact, the former has been derived from the mean value of the force signal, while the latter is from the amplitude of its oscillations. The extremely low frequency of the inputs ensures that inertial effects of the mass are negligible and force oscillations uniquely depend on dissipative phenomena.

The parameters of the test bench, i.e., the mass and LuGre friction model characteristic parameters [34], have been estimated, minimizing the RMS value of the error between the experimental and simulated data and obtaining a good fit.

5.3. Open Loop

Once the test bench components models are identified, the focus can be directed on the main system, i.e., the active damper. With the aim of minimizing the interconnected behavior of internal components and interrupting the backpropagation of disturbances and effects throughout internal loops within the system, a first campaign of tests has been carried out in an open loop configuration, entering into the system directly with a current input on the EHSV and measuring the generated force with the internal embedded load cell. By inhibiting the control logic, it is easier to understand the cascade of action/reaction phenomena occurring within the system without having to worry about differentiating the entities of the measured signal due to the system characteristics and that ascribed to the reaction of the controller to the given command or its seen disturbance.

The test results shown in Figure 13 have been obtained, maintaining the stimuli actuator active and steady in its null position, with the hydraulic brake disengaged and the

mass attached to the lower hinge of the damper. The ADV C, interposed between these two elements, has been tested with commands at different frequencies, namely 0.01 Hz (Figure 13a,b) and 1 Hz (Figure 13c,d). As previously mentioned, in this case, the extremely low frequency of inputs allowed the exclusion of inertial effects and concentration on the investigation of the governing phenomena in force generation. Hence, tests with a higher frequency helped to verify the fidelity of the model for different working conditions. The system showed few non-linearities for the 0.01 Hz case around the null force conditions, probably due to friction or internal leakages not considered by the mathematical model, which, in fact, struggled to reproduce this anomalous behavior. However, since the system was designed to operate at consistently higher frequencies, no modifications to the model structure have been introduced, taking into consideration the overall good fit of the simulated results with the measured force in other zones. Moreover, this behavior is not present in the case of 1 Hz input or higher frequencies, as will be shown in the next paragraphs.

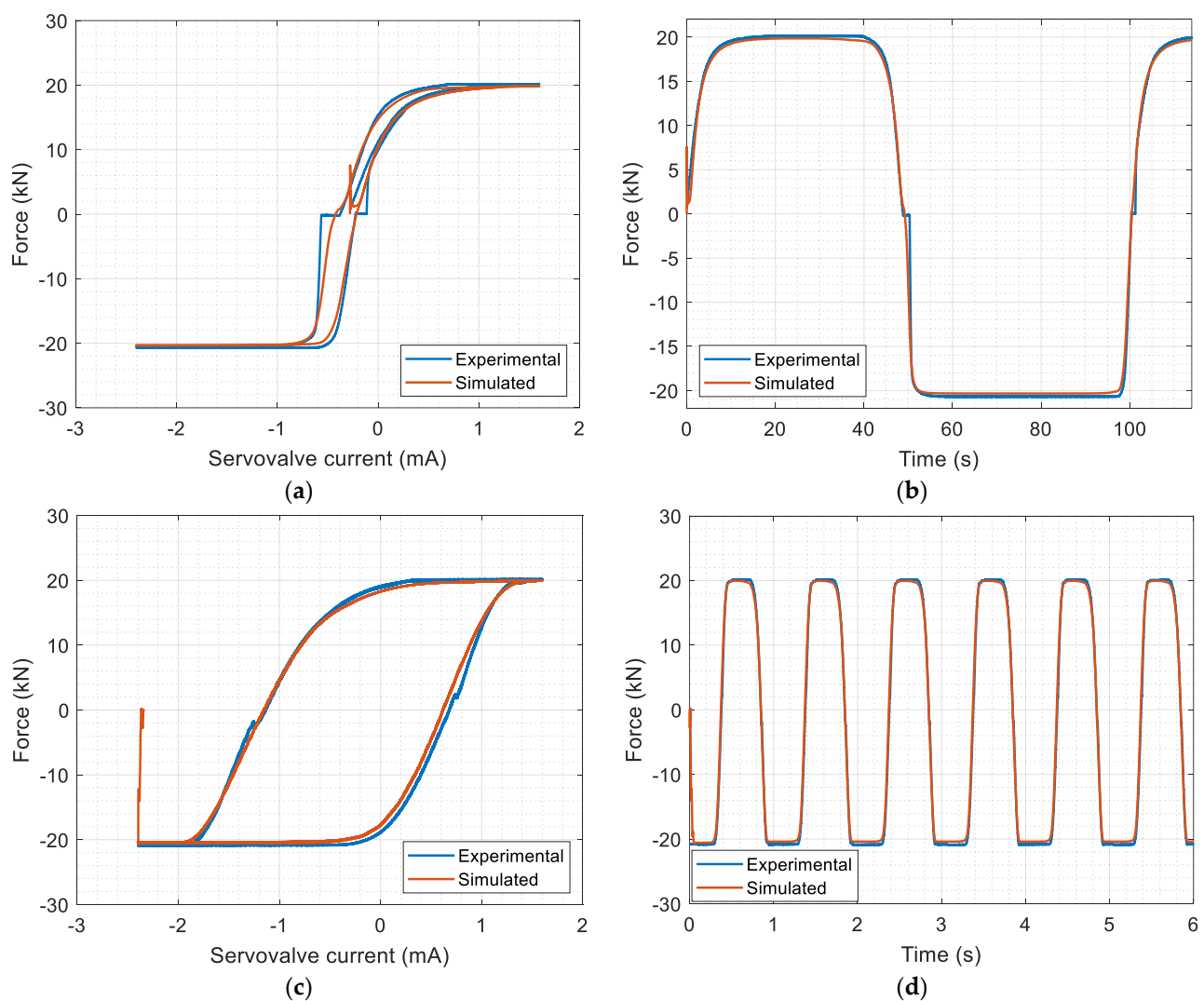


Figure 13. Results of the model parameter fitting process performed on experimental data from open loop tests with sinusoidal EHSV current inputs at (a,b) 0.01 Hz and (c,d) 1 Hz.

Some additional tests have been carried out disassembling the internal EHSA from the compliant strut and mounting it into a custom fixture appositely designed to block the movement of the rod to minimize the effect of the speed and, eventually, obtain useful insights into the system response to given inputs. The information obtained from these tests have been useful in understanding some behaviors of the system, diversifying the suite of measured sequences used in the parameter fitting process.

5.4. Closed Loop

Closed loop tests have been performed to investigate the effect of the control logic on the performance of the ADVC. Different experiments have been carried out with the stimuli actuator controlled in a fixed position, the hydraulic brake disengaged, and the suspended mass free to oscillate. To analyze the response of the system to different operating conditions and more robustly validate the model in various scenarios, several sinusoidal force requests have been supplied to the ADVC at the frequency of 25 Hz (the design point) with various force amplitudes [35] not related to the operative conditions typical of the specific helicopter class but only aimed at a better model parameters' identification.

The obtained simulated and experimental force signals for the cases of 1.5 kN, 3 kN, 5 kN, and 10 kN are shown in Figure 14, from which it is possible to note the ability of the mathematical model to accurately reproduce the main system dynamics and its non-linearities also for very different input conditions, confirming the effectiveness of the followed parameters identification procedure. Secondary oscillations are more demanding from the point of view of fidelity of reproduction, such as those exhibited by the real system for low input amplitudes.

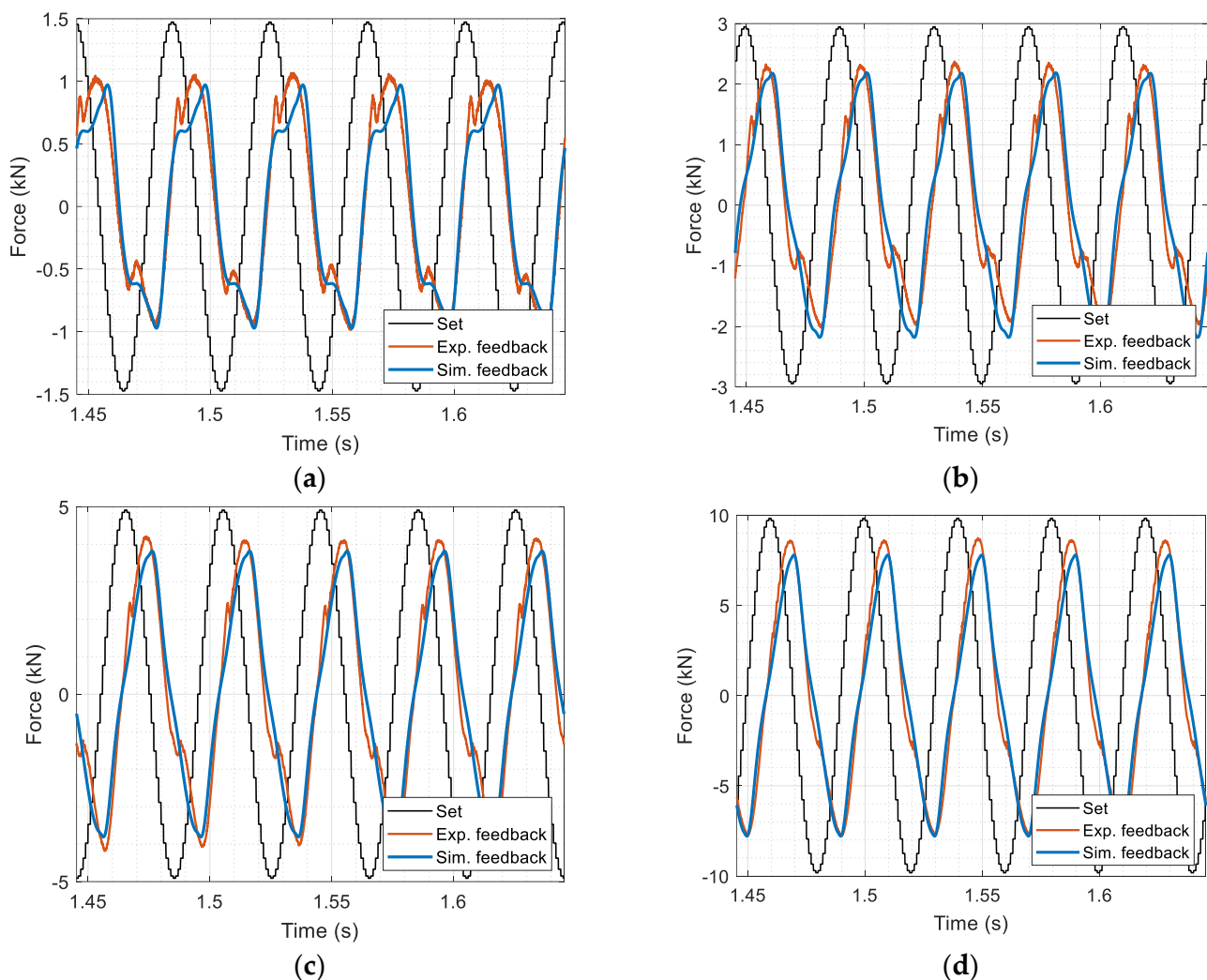


Figure 14. Results of the model parameter fitting process performed on experimental data from closed loop tests with steady stimuli actuator and 25 Hz sinusoidal force commands with amplitudes of (a) 1500 N, (b) 3000 N, (c) 5000 N, and (d) 10,000 N.

Nevertheless, the model, to some extent, succeeds in considering these oscillations, especially for negative forces. It is worth mentioning that the small force ripple occurring in

the acquired force signals before each peak, which becomes lower and lower with increasing set amplitudes, is mainly because the stimuli actuator is not blocked in a steady position, but it is position-controlled. Therefore, although dynamically rigid and robust, this actuator feels the effects of the force disturbance generated by the ADV C. It, therefore, reacts slightly to maintain its commanded steady position. It has been seen that its movement coincides with the small force oscillation occurring in the graphs. However, this behavior is not reproducible by the model as the stimuli actuator, as previously stated, is not modeled. However, its position is directly imposed as an input to the model as constraint coordinate and speed.

6. Experimental ATP Tests

This section concentrates on the presentation and examination of the experimental responses of the ADV C prototype to the dynamic tests of the ATP, which are the most important and interesting ones from the point of view of the ADV C performance and in view of its successive integration onboard helicopters. However, the Electrical Bonding Test is also part of the acceptance process.

The acceptance process involves two static tests to assess the compliant structure's stiffness and EHSA stall load. Furthermore, three dynamic tests evaluate the actuator's controllability and stability, displacement transmissibility, and ability to promptly respond to impulsive disturbances represented by a step displacement at the upper hinge. All the experiments have been carried out in the conditions specified by the ATP, i.e., with the MIL-PRF-83282 hydraulic fluid at $35 \pm 5^\circ\text{C}$, 207 ± 3 bar of supply pressure, and 7 ± 0.5 bar of return pressure.

The static tests are performed, keeping the stimuli actuator in a steady position. In the stall load test, the force request is slowly brought up to 125% of the theoretical stall load of the system both in compression and in extension. The generated force read by the internal load cell is monitored throughout the entire duration of the experiment. The result is positive if the maximum generated load distances from the nominal stall load is not less than -2.5% , i.e., if it stops above 19,500 N.

The second static test is aimed at verifying the stiffness of the external strut. The force command consists of a series of slow ramps to bring the load request up to 10 kN (50% of the stall load) both in compression and extension. Measuring both the hinges' displacements through the laser sensors and the created force by means of the internal load cell, the stiffness of the external structure is estimated. The test is considered passed if this value is in the range of $\pm 5\%$ of the theoretical value (i.e., 40 kN/mm), which means it must lie between 38 kN/mm and 42 kN/mm.

The ADV C prototype successfully passed both static tests, with the results listed in Table 3. The dynamic tests aim to evaluate and verify the dynamic capabilities of the ADV C, in particular, the controllability of the force loop, the transmissibility of the system, and the disturbance rejection features. The results of the dynamic tests are listed in Table 3.

Table 3. Results of the experimental ATP tests performed on the ADV C prototype.

Test	Pass Values	Results
Stall load	$F_{stall}^+ \geq 19,500\text{ N}$ $F_{stall}^- \leq -19,500\text{ N}$	20,890 N −20,630 N
Strut stiffness	$38.5 \leq k^+ \leq 42\text{ kN/mm}$ $38.5 \leq k^- \leq 42\text{ kN/mm}$	38.5 kN/mm 38.8 kN/mm
Controllability	$\left \frac{F_{fb}}{F_{set}} \right \geq -3\text{ dB@25Hz}$ $\angle \left(\frac{F_{fb}}{F_{set}} \right) \geq -90^\circ @25\text{Hz}$	−1.37 dB −65.4°
Transmissibility	$\left \frac{x_{LH}}{x_{UH}} \right \leq -6\text{ dB@25Hz}$ $\angle \left(\frac{x_{LH}}{x_{UH}} \right) \geq -70^\circ @25\text{Hz}$	−12.44 dB −39.0°
Step disturbance	$t < 50\text{ ms} : -200 \leq F \leq 200\text{ N}$	30.0 ms

The controllability of the system is evaluated with the stimuli actuator controlled in a fixed position and the electric brake open. Then, a sinusoidal force command at 25 Hz with an amplitude of $14 \pm 10\%$ kN is imposed on the EHSA controller. The procedure involves the evaluation of the attenuation and phase delay between the set and the measured force through the internal load cell: the test is passed if the feedback attenuation is lower than 3 dB and concurrently, the phase delay does not exceed 90° . Figure 15 shows the experimental and simulated results, which highlight that the real prototype fully satisfies the pass requirements, with an attenuation of only 1.37 dB and a phase delay of 65.4° . Moreover, it is also visible how the identified model successfully replicates the ADVC behavior, confirming the correctness of the identified parameter set.

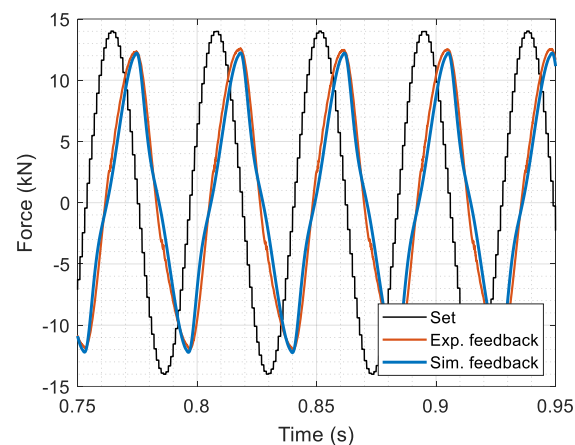


Figure 15. Experimental and simulated results of the ATP controllability test.

The transmissibility of the system constitutes the most informative test, directly showing the damping properties of the ADVC. Differently from the other tests, the stimuli actuator is not steady. However, it is commanded to generate a sinusoidal disturbance at the upper hinge at 25 Hz with an amplitude of $0.45 \pm 10\%$ mm. At the same time, a sinusoidal force set is given to the ADVC, conveniently phased with respect to the stimuli generator position set. In fact, the test is aimed to demonstrate the ADVC capabilities exploitable by the H/C designer, who, however, will be in charge of the control algorithm that generates the force set for the ADVC to suppress vibrations. During the ADVC ATP test, only a force control can be performed; therefore, this test follows an open loop approach to reduce the mass vibration [18]. A force set of 20 kN is imposed on the active damper (Figure 16a) with the aim of minimizing the vibration amplitude of the lower hinge, resulting in a vibration suppression of 12.44 dB with a phase delay of 39° , as shown in Figure 16b.

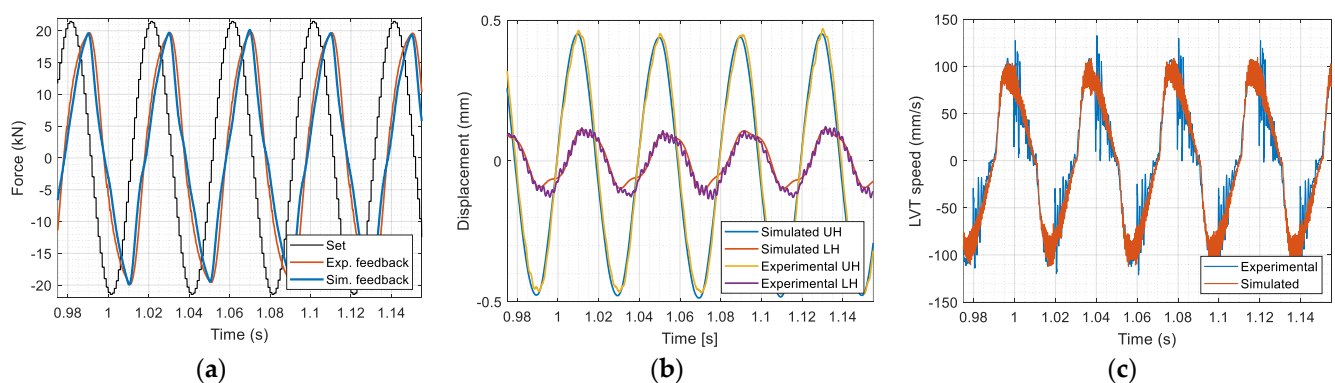


Figure 16. Experimental and simulated results of the ATP transmissibility test. (a) force, (b) hinge displacement, (c) relative speed between rod and cylinder.

The test is therefore passed, the obtained values being abundantly within the acceptability limits, i.e., a displacement attenuation greater than 6 dB with a phase delay lower than 70° . Figure 16 depicts the correspondence of the model results with measured signals in terms of hinge displacement and relative speed between the rod and the cylinder of the internal EHSA.

The final dynamic test of the ATP focuses on evaluating the ADVc capability to counteract external disturbances swiftly. The procedure entails commanding a zero-force input while introducing a step disturbance of 0.45 mm using the stimuli generator (orange in Figure 17).

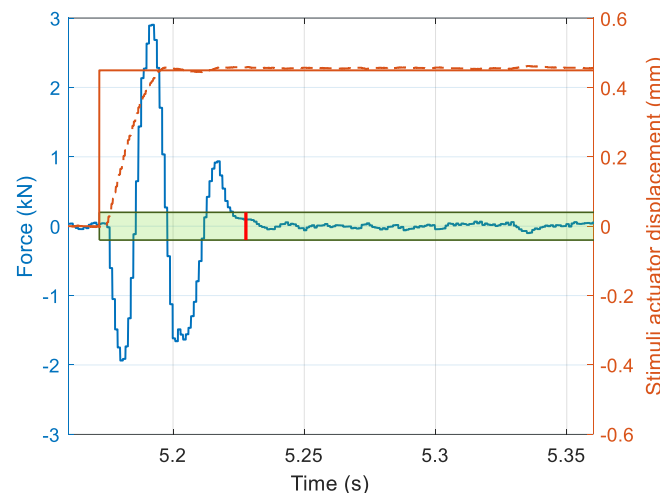


Figure 17. Experimental and simulated results of the ATP step disturbance test: the force signal in blue must enter the green acceptance region within 50 ms (red segment) from the disturbance displacement step appliance.

The objective is to measure the time it takes for the ADVc to restore the force (blue) within the acceptable range of ± 200 N (the shaded green area), with a specific time constraint of 50 ms from the end of the step disturbance. The time constraint is highlighted in Figure 17 by the red segment, representing 50 ms after the appliance of the step, to stay conservative. In reality, the stimuli actuator does not have an infinite acceleration, and it takes a certain amount of time to reach the ideal step position command: its real displacement is depicted with the orange dashed line. If the force restoring time is taken from the step appliance, the ADVc passes the test with a time of 30.0 ms.

7. Conclusions

This paper is the second part of a two-part work aimed at presenting the innovative solution presented by Elettronica Aster S.p.A. for the active damping of the vibrations generated by the main rotor/gearbox assembly in helicopters. Such vibrations are detrimental to onboard instrumentation and can lead to long-term pain for pilots and cabin occupants.

The proposed solution is to replace the supporting rigid struts, i.e., the principal vibration transmission path, with active dampers in charge of attenuating the vibration level. The latter consists of an electro-hydraulic servo-actuator in parallel with a compliant structure responsible for bearing the static load. This layout allows the entire system to achieve an extremely high power density compared to similar solutions while keeping the mass and dimensions contained. Part 1 presented the layout of the system, the mathematical model, and the model-based design. The mathematical model was used to preliminary validate the design, confirming the compliance of the defined solution to the ATP requirements.

Part 2 builds upon the findings of Part 1, presenting the damper prototype's physical realization, the experimental rig appositely designed to perform ATP certification tests and the results of the experimental campaign. In particular, an extensive step-by-step discussion on mathematical model validation and parameter tuning has been carried out. The model

has been used to optimize the control parameters to achieve the required performance. Furthermore, it has been a valuable tool in the initial phase to verify the correspondence of the system response with the expected behavior.

The comprehensive analysis and evaluation conducted in this study highlight the successful implementation and performance of the active damper prototype, which successfully passed all ATP tests. In conclusion, the experimental findings presented in this paper demonstrate the effectiveness and potential of the proposed active damper solution for effectively mitigating vibrations in the given application, improving operational efficiency, and increasing both the service life of the targeted system and the flight quality perceived by cabin passengers.

Future work will focus on optimizing the control parameters of the active damper to enhance its capabilities, for example, enhancing feedforward branches exploiting the LVT signal. Furthermore, the manufacturing of additional prototypes of the active damper will help to improve the statistical significance and further validate the performance and reliability of the proposed solution across a larger sample size. This comprehensive and robust analysis will allow for a deeper understanding of the performance and reliability of the ADV, providing valuable insights into the consistency and effectiveness of the proposed solution across multiple instances, therefore strengthening the overall validity and generalizability of the results.

Author Contributions: Conceptualization, A.C.B., M.G., P.G.P. and S.S.; methodology, A.C.B.; software, A.C.B.; validation, A.C.B. and S.S.; formal analysis, A.C.B. and S.S.; investigation, A.C.B. and S.S.; resources, A.C.B.; data curation, A.C.B.; writing—original draft preparation, A.C.B.; writing—review and editing, A.C.B., M.G., S.S., P.G.P. and M.S.; visualization, A.C.B.; supervision, P.G.P. and M.S.; project administration, S.S., P.G.P. and M.S.; funding acquisition, P.G.P. and M.S. All authors have read and agreed to the published version of the manuscript.

Funding: This research was partially funded by the Italian Ministry of Defense under the National Program for Military Research (PNRM), grant number n° 806 di Rep. del 04.05.2016.

Data Availability Statement: Data sharing is not applicable to this article.

Conflicts of Interest: The funders had no role in the design of the study, in the collection, analyses, or interpretation of data, in the writing of the manuscript, or in the decision to publish the results.

References

1. Viswamurthy, S.R.; Ganguli, R. Performance sensitivity of helicopter global and local optimal harmonic vibration controller. *Comput. Math. Appl.* **2008**, *56*, 2468–2480. [\[CrossRef\]](#)
2. Tamer, A.; Muscarello, V.; Masarati, P.; Quaranta, G. Evaluation of vibration reduction devices for helicopter ride quality improvement. *Aerosp. Sci. Technol.* **2019**, *95*, 105456. [\[CrossRef\]](#)
3. Tamer, A.; Zanoni, A.; Cocco, A.; Masarati, P. A numerical study of vibration-induced instrument reading capability degradation in helicopter pilots. *CEAS Aeronaut. J.* **2021**, *12*, 427–440. [\[CrossRef\]](#)
4. De Oliveira, C.G.; Nadal, J. Transmissibility of helicopter vibration in the spines of pilots in flight. *Aviat. Space Environ. Med.* **2005**, *76*, 576–580. [\[PubMed\]](#)
5. McFarland, J.M.; Riha, D.S. Uncertainty quantification methods for helicopter fatigue reliability analysis. In Proceedings of the Annual Forum Proceedings—AHS International, Grapevine, TX, USA, 27–29 May 2009; Volume 3, pp. 2730–2737.
6. Chee Tong, Y.; Antoniou, R.A.; Wang, C.H. Probabilistic Fatigue Life Assessment For Helicopter Dynamic Components. In Proceedings of the Structural Integrity and Fracture (SIF), Brisbane, Australia, 26–29 September 2004.
7. Konstanzer, P.; Enenkl, B.; Aubourg, P.A.; Cranga, P. Recent advances in Eurocopter's passive and active vibration control. In Proceedings of the Annual Forum Proceedings—AHS International, Montreal, QC, Canada, 29 April–1 May 2008; Volume 1, pp. 854–871.
8. Kryszinski, T.; Malburet, F. *Mechanical Vibrations—Active and Passive Control*, 2nd ed.; ISTE Ltd.: London, UK, 2021; ISBN 9781905209293.
9. Pearson, J.T.; Goodall, R.M.; Lyndon, I. Active control of helicopter vibration. *Comput. Control Eng. J.* **1994**, *5*, 277–284. [\[CrossRef\]](#)
10. Welsh, W.A. Helicopter Vibration Reduction. In *Morphing Wing Technologies: Large Commercial Aircraft and Civil Helicopters*; Elsevier Ltd.: Stratford, CT, USA, 2018; pp. 865–892.
11. Yang, R.; Gao, Y.; Wang, H.; Ni, X. Reducing Helicopter Vibration Loads by Individual Blade Control with Genetic Algorithm. *Machines* **2022**, *10*, 479. [\[CrossRef\]](#)

12. Cresap, W.L.; Myers, A.W.; Viswanathan, S.P. Pylon Mounting System for Reducing Helicopter Vibration. U.S. Patent 4,362,281, 7 December 1982.
13. Rodriguez, J.; Cranga, P.; Chesne, S.; Gaudiller, L. Hybrid active suspension system of a helicopter main gearbox. *JVC/J. Vib. Control* **2018**, *24*, 956–974. [\[CrossRef\]](#)
14. Lang, K.; Xia, P. Hybrid active vibration control of helicopter fuselage driven by piezoelectric stack actuators. *J. Aircr.* **2019**, *56*, 719–729. [\[CrossRef\]](#)
15. Meng, D.; Xia, P.; Song, L.; Smith, E.C. Experimental study on piezoelectric-stack-actuator-driven active vibration control of helicopter floor structure. *J. Aircr.* **2020**, *57*, 377–382. [\[CrossRef\]](#)
16. Staple, A.E.; Wells, D.M. The development and testing of an active control of structural response system for the EH101 helicopter. In Proceedings of the 16th European Rotorcraft Forum, Glasgow, UK, 18–20 September 1990.
17. King, S.P.; Hughes, C.I. Method and Apparatus for Reducing Vibration of a Helicopter Fuselage. U.S. Patent 4,819,182, 4 April 1989.
18. Bertolino, A.C.; Gaidano, M.; Smorto, S.; Porro, P.G.; Sorli, M. Development of a High-Performance Low-Weight Hydraulic Damper for Active Vibration Control of the Main Rotor on Helicopters—Part 1: Design and Mathematical Model. *Aerospace* **2023**, *10*, 391. [\[CrossRef\]](#)
19. Trans-Tek Inc. Linear Velocity Transducers Series 100 Catalog 2023, Ellington, CT, USA. Available online: <https://transtekinc.com/> (accessed on 19 June 2023).
20. MOOG Inc. 30 Series Servo Valves datasheet—Direct-Operated Flow Control for Analog Signals Micro-Hydraulics 2023, East Aurora, NY, USA. Available online: <https://www.moog.com/products/servo-valves-servo-proportional-valves/industrial/flow-control/analog-without-integrated-electronics/30-series-flow-control-servo-valve.html> (accessed on 19 June 2023).
21. Quaternion Solutions Inc. *Nonelectronic Parts Reliability Data (NPRD-16)*; 13502-1311; Quaternion Solutions Inc.: Utica, NY, USA, 2016.
22. Trelleborg Sealing Solutions Aerospace Sealing Systems—Product catalog & Engineering Guide 2011, Johan Kocksgatan 10, Trelleborg, Sweden. Available online: <https://www.trelleborg.com/en/seals/resources/catalogs-and-brochures> (accessed on 19 June 2023).
23. Precision Rings Incorporated Custom Piston Ring Manufacturing Solutions. 2023. Available online: <https://www.precisionrings.com/> (accessed on 19 June 2023).
24. The Lee Company Product catalog 2023, Westbrook, CT, USA. Available online: <https://www.theleeco.com/products/> (accessed on 19 June 2023).
25. HBM U10M Force Transducer catalogue 2022, Darmstadt, Germany. Available online: https://www.hbm.com/en/2410/u10-ultra-precision-load-cell-the-reliable-choice/?product_type_no=U10%20Ultra%20Precision%20Load%20Cell:%20The%20reliable%20choice (accessed on 19 June 2023).
26. Keyence International Ultra High-Speed/High-Accuracy Laser Displacement Sensors catalogue—LKG5000 series 2023, Itasca, IL, USA. Available online: <https://www.keyence.com/products/measure/laser-1d/lk-g5000/> (accessed on 19 June 2023).
27. Idelchik, I.E. *Handbook of Hydraulic Resistance*; Begell House Inc.: Moscow, Russia, 2007; ISBN 9781567002515.
28. Merrit, H.E. *Hydraulic Control Systems*; John Wiley & Sons, Inc.: New York, NY, USA; London, UK; Sydney, Australia, 1967; ISBN 0471596175.
29. De Martin, A.; Dellacasa, A.; Jacazio, G.; Sorli, M. High-Fidelity Model of Electro-Hydraulic Actuators for Primary Flight Control Systems. In Proceedings of the BATH/ASME 2018 Symposium on Fluid Power and Motion Control, Bath, UK, 11–13 September 2018; American Society of Mechanical Engineers: Bath, UK, 2018; pp. 1–8.
30. Jelali, M.; Kroll, A. *Hydraulic Servo-Systems: Modeling, Identification and Control*; Springer Ltd.: London, UK, 2003; ISBN 978-1-4471-0099-7.
31. Bertolino, A.C.; De Martin, A.; Jacazio, G.; Sorli, M. A Case Study on the Detection and Prognosis of Internal Leakages in Electro-Hydraulic Flight Control Actuators. *Actuators* **2021**, *10*, 215. [\[CrossRef\]](#)
32. Bertolino, A.C.; Gentile, R.; Jacazio, G.; Marino, F.; Sorli, M. EHSA Primary Flight Controls Seals Wear Degradation Model. In Proceedings of the IMECE2018, Pittsburgh, PA, USA, 9–15 November 2018; ASME: New York, NY, USA; pp. 1–12.
33. Thayer, W.J. Specification standards for electrohydraulic flow control servovalves. *MOOG Tech. Bull.* **1962**, *117*, 152–154. [\[CrossRef\]](#)
34. Ruderman, M.; Bertram, T. Two-state dynamic friction model with elasto-plasticity. *Mech. Syst. Signal Process.* **2013**, *39*, 316–332. [\[CrossRef\]](#)
35. Bertolino, A.C.; Smorto, S.; Porro, P.; Sorli, M. A low weight electro-hydraulic active damper to control main rotor vibrations on helicopters. In Proceedings of the International Conference on Electrical, Computer, Communications and Mechatronics Engineering, ICECCME23, Tenerife, Canary Islands, Spain, 19–20 July 2023; pp. 19–20.

Disclaimer/Publisher’s Note: The statements, opinions and data contained in all publications are solely those of the individual author(s) and contributor(s) and not of MDPI and/or the editor(s). MDPI and/or the editor(s) disclaim responsibility for any injury to people or property resulting from any ideas, methods, instructions or products referred to in the content.